Cite as:

Pepe J, Cleven L, Suijkerbuijk E, Dekkers E, Hermida-Merino D, Cardinaels R, Peters G, Anderson P, A filament stretching rheometer for in-situ X-ray experiments: Combining rheology and crystalline morphology characterization, Rev. Scient. Instruments 91, 073903 (2020) https://doi.org/10.1063/5.0008224

A filament stretching rheometer for *in-situ* X-ray experiments: combining rheology and crystalline morphology characterization

Jessica Pepe,[1,2] Lucien C. Cleven,[1] Eduard J. M. C. Suijkerbuijk,[3] Erwin C. A. Dekkers,[3] Daniel Hermida-Merino,[4] Ruth Cardinaels,[1] Gerrit W. M. Peters,[1] and Patrick D. Anderson[1, a)]

[1)]*Polymer Technology, Department of Mechanical Engineering, Eindhoven University of Technology, P.O.Box 513, 5600 MB Eindhoven, The Netherlands*

[2)]*Brightlands Materials Center, 6167 RD, Geleen, The Netherlands*

[3)]*Equipment & Prototyping Center, Eindhoven University of Technology, P.O.Box 513, 5600 MB Eindhoven, The Netherlands*

[4)]*DUBBLE CRG BM26 at ESRF Netherlands Organization for Scientific Research (NWO), 71 Avenue des Martyrs, 38000 Grenoble, France*

ABSTRACT

We present a rheometer that combines the possibility to perform *in-situ* X-ray experiments with a precise and locally controlled uniaxial extensional flow. It thus allows to study the crystallization kinetics and morphology evolution combined with the rheological response to the applied flow field. A constant uniaxial deformation rate is ensured thanks to a fast control scheme that drives the simultaneous movement of the top and bottom plate during a pulling experiment. A laser micrometer measures the time evolution of the smallest diameter, where the highest stress is concentrated. The rheometer has a copper temperature-controlled oven with the ability to reach 250°C and a N_2 connection to create an inert atmosphere during the experiments. The innovation of our rheometer is the fixed location of the midfilament position, which is possible because of the simultaneous movement of the two end plates. The copper oven has been constructed with four ad-hoc windows: two glass windows for laser access and two kapton windows for X-ray access. The key feature is the ability to perfectly align the midfilament of the sample to the laser micrometer and to the incoming X-ray beam in a synchrotron radiation facility, allowing to investigate structure and morphologies developed during extensional flow. The rheological response measured with our rheometer for LDPE is in agreement with the linear viscoelastic envelope and with the results obtained from existing extensional rheometers. To demonstrate the capability of the instrument we have performed *in-situ* time-resolved X-ray experiments on LDPE samples exhibiting extensional flow-induced crystallization.

[a)]p.d.anderson@tue.nl

I. INTRODUCTION

Nowadays, polymers, and in particular thermoplastics, are widely used materials in the manufacturing industry, thanks to their relatively low price, good processability and wide range of achievable properties. Despite these favorable aspects polymers are quite elaborate molecules and, as a consequence their response to the thermo-mechanical history experienced during processing is not only complex, but also different from one polymer to the other. During processing, using techniques ranging from the most consolidated ones, like extrusion, injection molding, blow molding and fiber spinning, to the emerging ones such as filament fused deposition modeling (FDM) and inkjet printing, polymers are subjected to various flow fields, consisting of both shear and extensional contributions. For semi-crystalline materials the presence of flow largely affects the kinetics as well as formed crystal morphologies and structures[1–3] which in turn affect the final properties (e.g. mechanical, optical, barrier, piezoelectrical)[4–6]. It is well-established that the most common crystalline morphology developed during strong flows is the so called "shish-kebab" consisting of: extended crystal chains oriented in the direction of the flow (shish), and folded chain lamellae in the opposite direction (kebab)[2]. Shear-induced crystallization has received substantial attention since decades[7]. Thereto, several innovative setups and modifications of existing setups that allow *in-situ* crystallization studies have been developed. These devices were combined with various *in-situ* structure characterization techniques, like birefringence[8–11], optical imaging[12,13], X-ray scattering and diffraction (SAXS, WAXD)[2,14–18]. In the context of flow-induced crystallization time resolved X-ray experiments are the most popular technique to resolve the structure evolution during processing[19–24].

Despite the extreme importance of extensional flow in polymer processing, very little is known about the material response to an extensional flow and even less is known about extensional flow-induced crystallization. This is because the implementation of an ideal uniaxial extensional deformation is still an experimental challenge and there is a lack of suitable devices for the application of uniaxial extensional flow combined with *in-situ* characterizations. Nevertheless several studies have been conducted in order to understand the role of extensional flow in the crystallization process[25–40]. They use different devices that either generate a precise and locally controlled uniaxial extension resulting in accurate rheological data without *in-situ* access to the microstructure[25–33], or they facilitate *in-situ* structure characterization whereas the deformation field undergone by the material is less well controlled[34–40]. In the former category a commercial

(VADER 1000) and a home-built filament stretching rheometer have been used, to study the extensional flow-induced crystallization of a commercial low density polyethylene (LDPE) and an isotactic polypropylene (iPP) respectively[30,32,33]. The filament stretching rheometer is a powerful and versatile tool to investigate the extensional rheology of complex fluids with a wide range of viscosities and it allows to reach high strains. It mainly consists of two plates, of which one moves, thereby stretching the fluid in between. The most important feature of this type of device is its ability to keep the deformation rate at the midfilament point constant, leading to an ideal uniaxial extensional flow. In both devices only the upper plate moves causing a shift of the middle point position over time, that allows only for structure characterization via post-mortem *ex-situ* X-ray experiments. In the second category, apart from cross-slot flow cells[34–36], a home-built double-drum windup device allows for *in-situ* X-ray characterization during extension and has been tested on poly(ethylene oxide), poly(1-butene) and a commercial iPP [37–40]. This rheometer has two counter-rotating drums as in the Sentmanat extensional add-on for commercial shear rheometers (SER)[41] with improved design to reduce polymer sagging and to homogenize the temperature. However this type of rheometer is limited in the Hencky strain values that can be reached and it does not allow for local strain (rate) measurements or control. A homogeneous deformation is assumed, which is however not always the case, especially at large values of the Hencky strain, as shown in the study of McCready et al.[42] on pre-aligned cylindrical block copolymer melts.

In the current work we present, for the first time to our knowledge, a rheometer that combines the possibility to perform *in-situ* X-ray characterization whilst the material undergoes a precise and locally controlled uniaxial extensional flow. The general design of the rheometer is based on existing filament stretching rheometers[43–46], but differs from that of similar devices in its ability to perform *in-situ* experiments while locally controlling the deformation. To fulfill this purpose the design of the rheometer ensures the stationary position of the midfilament point allowing precise alignment of it to the X-ray source. An electrically heated oven is built to control the temperature and degradation is avoided using nitrogen gas. Studies of polymer crystallization, combining scattering (SAXS) and diffraction (WAXD) techniques, with this device will allow us to develop an understanding of the extensional flow-induced crystallization process.

II. RHEOMETER DESIGN AND DESCRIPTION

Fig. 1 shows the rheometer combined with SAXS/WAXD measurements, as arranged in the beamline. A 3D virtual reality model can be found in the supplementary material.

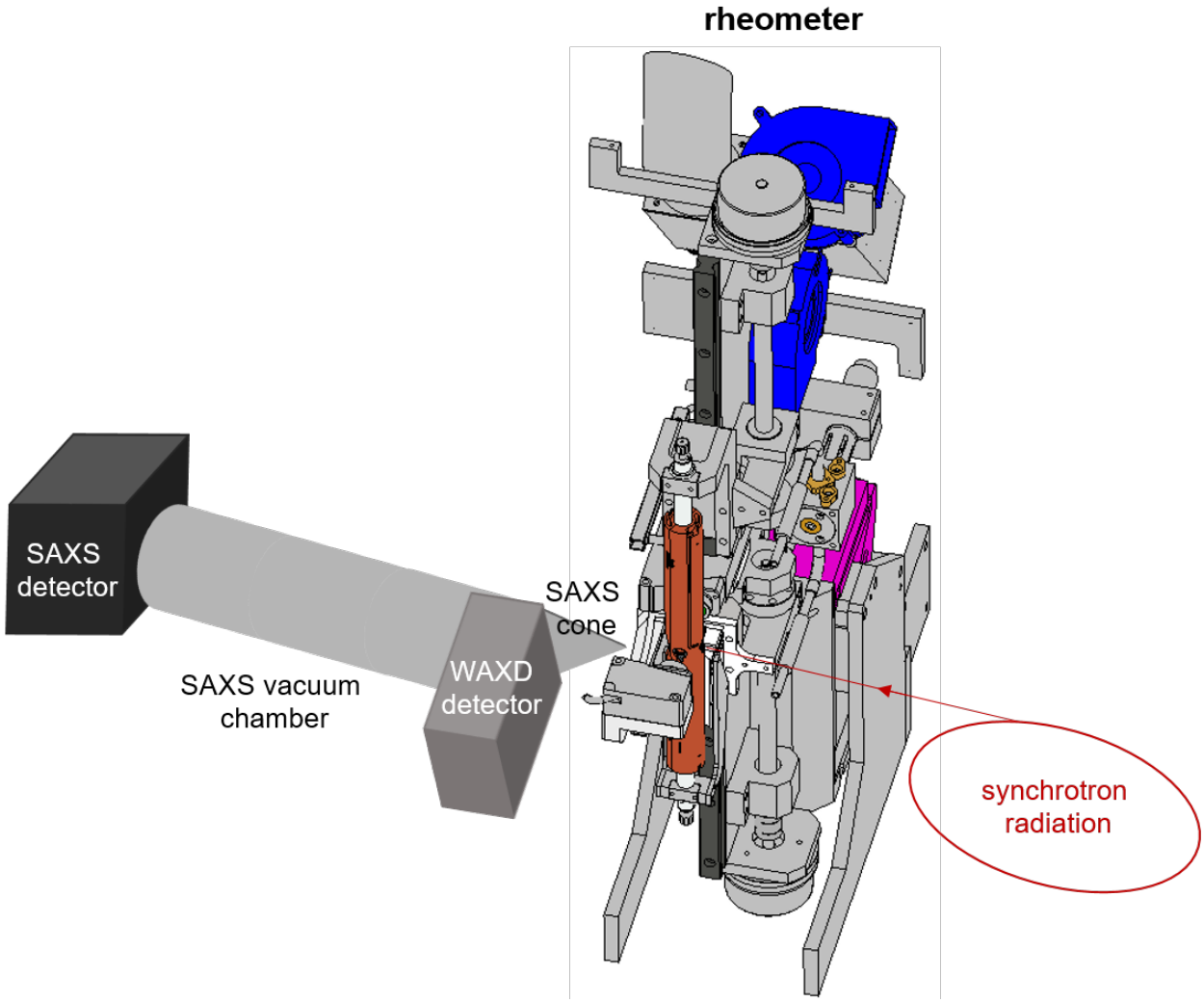

FIG. 1. Schematic of the experimental setup with *in-situ* X-ray capability, as placed in the ESRF beamline.

The rheometer is constructed with two end plates that move simultaneously and at the same velocity (Fig. 2 (a)), the latter being controlled to create an ideal uniaxial extensional deformation. In an ideal uniaxial extensional flow at a constant strain rate the length increases and the diameter decreases exponentially in time. To control the deformation at the midpoint the diameter is constantly measured by a laser micrometer and its value serves as input for a closed control loop. The simultaneous movement of the plates is realized by two motors driven by two ball screws that are

independently controlled. The response of the material to the deformation is measured by a load cell connected to the bottom plate. An *ad-hoc* copper oven allows for high temperature experiments in an inert environment, and enables access for the laser micrometer and the X-ray source. The four windows, two for the laser and two for the X-rays (Fig. 2 (c)), are aligned with respect to each other with an accuracy of $\pm 50\ \mu$m, ensuring a precise alignment of the midfilament point to the laser and subsequently to the X-ray beam, as will be described in detailed later. Fig. 2 (b) and Fig. 2 (d) show the rheometer with the main components indicated. The overall programming and controlling of the filament stretching rheometer is done with MATLAB® Simulink. The RTI1104 DSpace® card is the real time control platform that runs the model created in Simulink, while DSpace® ControlDesk software provides a user interface to interactively work with the model. The main components and features are described in more detail in the following sections.

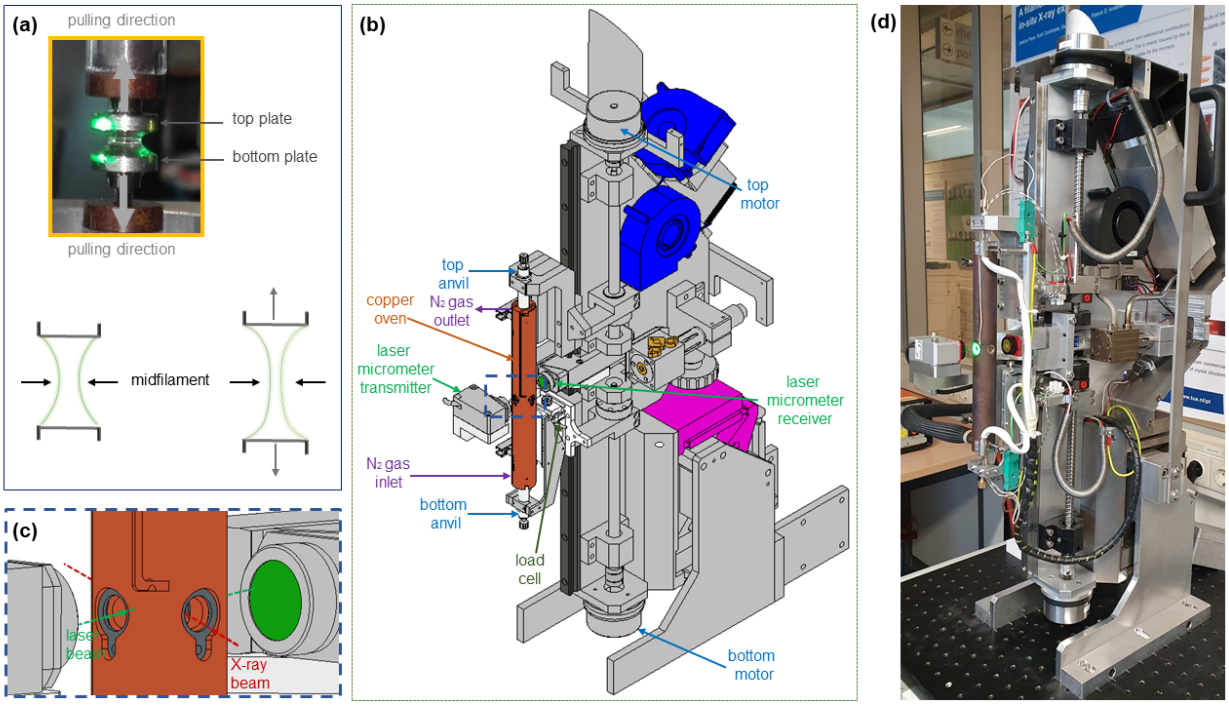

FIG. 2. (a) Picture of a pre-stretched sample between top and bottom plate, pulling direction is indicated by the arrows and schematic of the diameter evolution with the midfilament point stationary in time. (b) 3D drawing of the in-house developed filament stretching rheometer. (c) Zoomed-in view of the oven showing the alignment of the four windows and the direction of the laser and the X-ray beam. (d) Photograph of the device.

A. Motion control and force measurement

The top and bottom stainless steel plates are connected to two pistons thanks to their threaded body. Hence it is possible to use, and easily interchange plates of different diameters, materials and geometries, which allows to increase the contact between the sample and the plates in case slip-off occurs[33]. Each piston consists of two main components, a copper plate holder in which the plates are screwed and a quartz tube that accommodates the plate holder itself, the heating element and the thermocouple used to heat and control the temperature of the plates, respectively, as shown in Fig. 3. The low thermal expansion coefficient of quartz ensures minimum changes in length and thus minimum changes in the position of the plates.

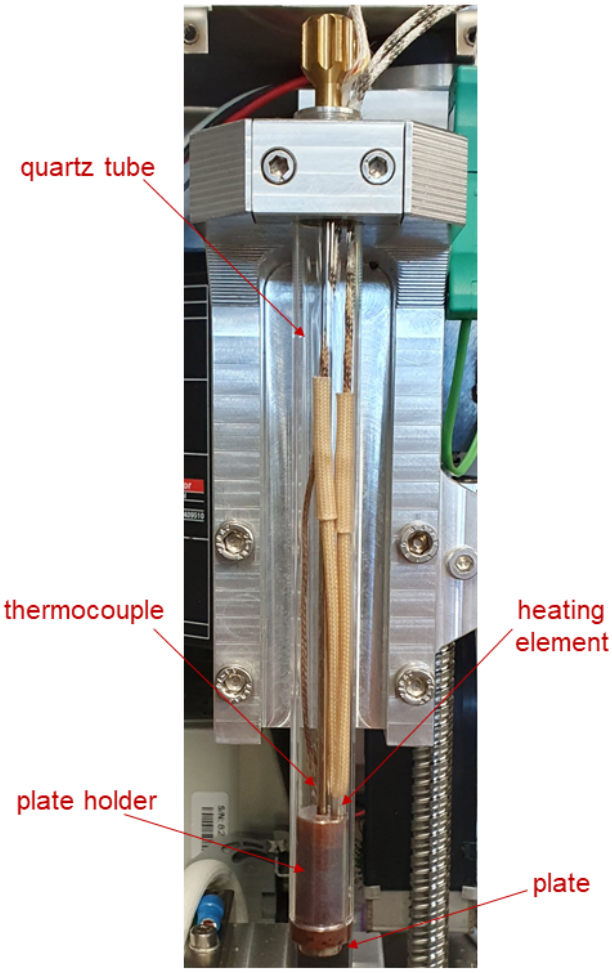

FIG. 3. Photograph of the piston with its components indicated.

The pistons are mounted and connected to a preloaded linear profile guide that is linked by ball

screws to the motors. The maximum distance achievable between the plates is 145 mm. When the oven is used, this distance is reduced to 114 mm to assure that the pistons always remain inside the oven, throughout the experiment. The motors that drive the guides are EC Maxon motors, with a maximum speed of 3740 rpm, which corresponds to a maximum linear movement of 623.3 mm/s for a single axis, while the minimum speed is 0.001 mm/s. The motors are externally controlled by a servocontroller, an encoder provides the electrical signal that is used for speed control. The sampling time of the speed controller is 200 μs.

The axial force on the bottom plate during the uniaxial experiment is measured by a load cell HBM U9C of 100N maximum nominal force. The load cell housing is designed as such that different cells can easily be interchanged (i.e. to measure lower viscous samples). In particular 2N and 20N (XFTC300) load cells are available. The load cell has been calibrated both in compression, by placing known weights on it, and in tension, by pulling, at constant rate, a metallic spring of which the elastic constant k is known. The calibration indicated that the minimum value measurable by the 100N load cell is 0.02 N with a noise level of $\pm$0.01 N. Furthermore it was verified that the contribution of the acceleration from the moving components to the total force measured during an experiment is negligible. The load cell is placed outside the oven to ensure that no increase of its temperature occurs during the experiments.

At the center of the oven there are two flat quartz windows providing optical access for the head and receiver of the KEYENCE LS-9006 laser micrometer, thereby allowing it to measure the diameter of the sample during the experiment. Because the middle point location of the polymer is fixed, the laser, mounted on an aluminum support, is aligned to the oven quartz windows and, thus, to the midfilament point. The measurable diameter ranges from 0.04 mm to 6 mm, with an accuracy of $\pm$ 0.5 µm. For a typical initial sample diameter $D = 5$ mm and height $L = 1.5$ mm, the combination of laser micrometer range and motor speed results in a maximum Hencky strain of 9 and extension rates ranging from 0.00001 s^{-1} to 5 s^{-1}. The aluminum support on which the laser is mounted allows to dissipate the heat generated from the laser itself and to keep it within its operating temperature range. The laser micrometer not only measures the diameter but also shows video images of the measured area (over a filament height of 1.6 mm), allowing to verify the location of the minimum diameter.

B. Oven

Around the pistons a cylindrical copper oven is constructed to control the temperature and to create an inert atmosphere, and its design is crucial for the success of the *in-situ* X-ray experiments. The copper oven is designed as a double wall cylinder with an external diameter (D_e) of 38 mm and an internal diameter (D_i) of 13 mm. Copper is chosen as construction material because of its high thermal conductivity and because it can easily be shaped. Dimensional choices are restricted by the requirements of good temperature control, minimal amount of air around the sample to minimize the scattering background, and correct placement of the rheometer in the beamline. The internal diameter has been chosen as the minimum possible value in order to reduce the gap between the quartz tube and the copper oven, and to minimize the scattering background coming from the air. The outer diameter is the optimal compromise between design limitations and the beamline requirements of placing the rheometer as close as possible to the incoming tube of the X-ray source and to the SAXS cone to reduce the background scattering. In order to allow an X-ray beam to access the oven and to collect all the diffraction and scattering patterns from the polymer two Kapton windows of 0.05 mm thick have been designed as shown in Fig. 4 (b). Kapton is the material of choice because, being amorphous, it is free of strong diffraction peaks and it does not show lamellar scattering in the q-range of our interest. The inlet window for the X-ray beam has a diameter of 6 mm, as the two quartz windows for the laser access. The window for the outlet of the X-ray beam has been realized with an intrusive angle of 90° facilitating diffraction angles (2θ) of most polymeric materials.

Eight heating rods with a power of 100 W each, four on the top and four at the bottom equally distributed on all sides in the oven walls, regulate the temperature of the oven (Fig. 4 (a)). In order to avoid degradation of the polymer because of the high temperatures involved, nitrogen gas (at a pressure of 1 bar) continuously flows from the bottom through the oven keeping the environment inert and helping in reducing temperature gradients. The nitrogen gas is externally preheated using a 400 W heating cartridge regulated by a thermocouple and Hasco power supply unit. The heat is transferred to the polymer from the plates by conduction and from the heated nitrogen in the oven by convection. The temperature is measured and controlled in three points: at the top and bottom plate and in the oven wall at the center of the oven, where K-type thermocouples (RS Pro, ± 1 °C accuracy) are integrated. Three feedback loops regulate the temperature of the plates

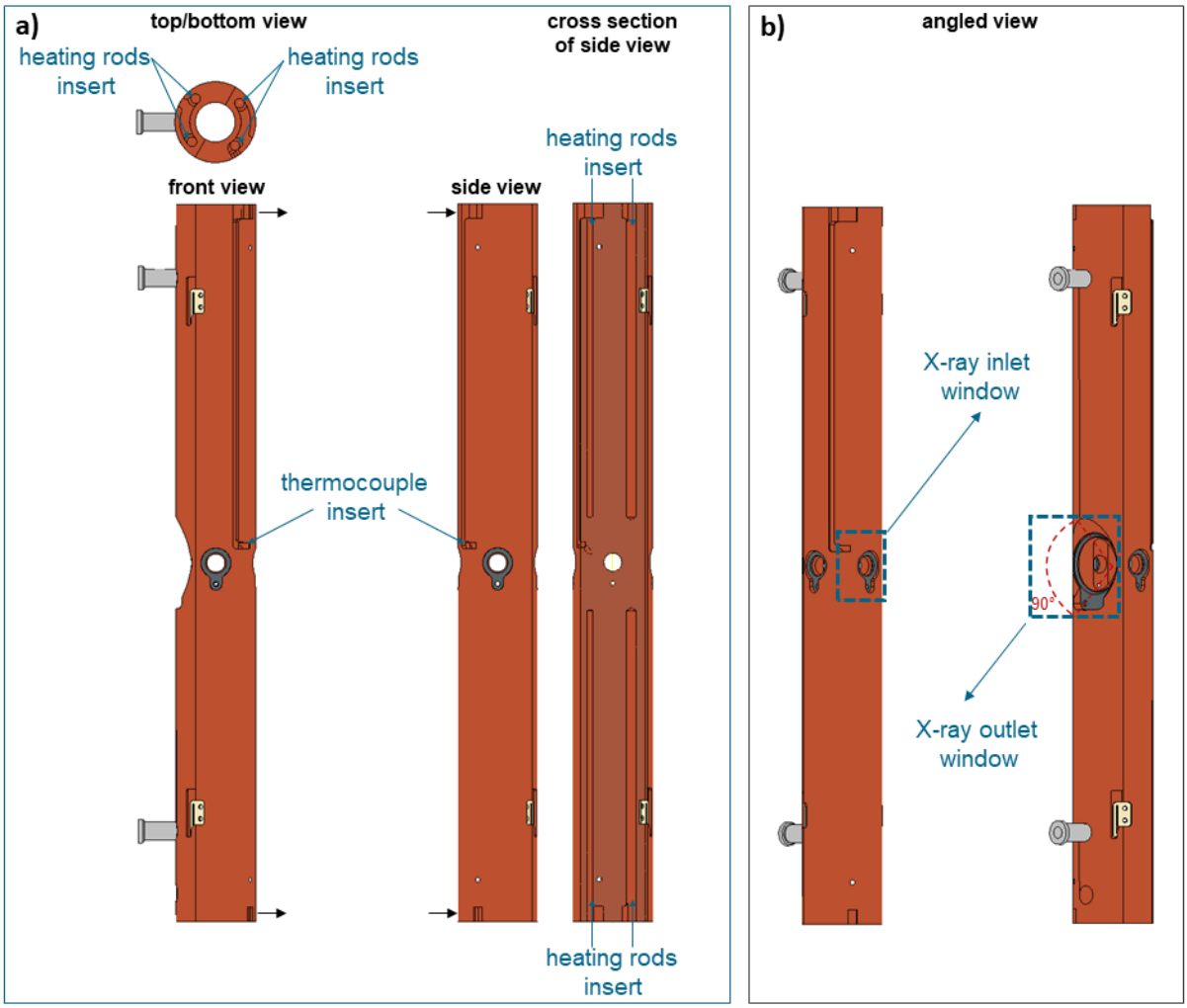

FIG. 4. Technical drawing of the oven. (a) Top/bottom, front and side views with thermal insert. Cross-section and top/bottom view show the heating inserts. (b) Angled view of the inlet and outlet windows for the X-rays.

and of the oven using the three independently measured temperatures as input values. Each loop contains a PI controller. The temperature of the sample at the middle point has been checked with an external thermocouple, of the same type as mentioned before and placed directly into the polymer. The found temperature offset from the set point is 5°C (corrected for during the experiments) and the maximum achievable temperature is 250 °C. The heating and cooling rate are fixed, and approximately 100°C/min and 4°C/min, respectively. There is an overshoot of 2°C and the oscillations around the set point are ±0.5°C. We chose to not cover the copper oven with an insulation shield because the presence of insulation would enormously increase the cooling time, which is extremely undesired for flow-induced crystallization experiments.

C. Control scheme implementation

In this type of rheometer a perfect uniaxial extensional deformation is not achievable throughout the filament because of the presence of the rigid plates. The contact with the end plates results in deviations from a cylindrical shape due to which the average and local extension rates differ from each other. In early version of filament stretching rheometers, a locally constant uniaxial extension rate was accomplished by determining the plate speed evolution via trial-and-error, which gave good control for polymer solutions[43,47]. When using polymer melts the implementation of open control loops becomes a tedious process due to the dependence of the material rheology on the strain rate[48]. Previous works show that by means of an active real time control of the diameter evolution at the midfilament point, it is possible to impose, locally, a deformation at constant rate and thus to achieve an ideal uniaxial extensional flow[48,49]. The most successful way to perform such experiments is to implement a closed control loop, and the most robust algorithm available at present for controlling the kinematics of a filament stretching rheometer is the one proposed by Marín et al.[48]. The working principle of this control scheme is schematically depicted in Fig. 5.

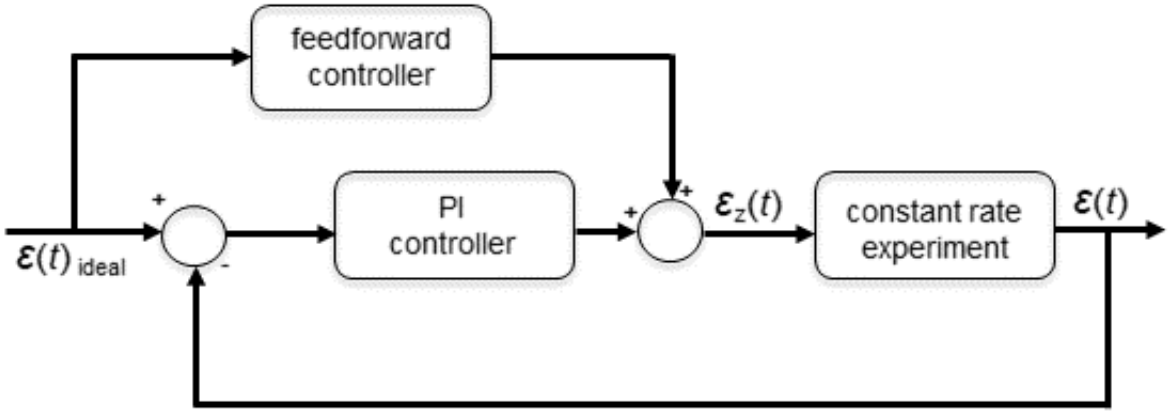

FIG. 5. Schematic of the control scheme.

In the control loop the Hencky strain based on diameter (ε) is the controlled variable:

$$\varepsilon = -2\ln\left(\frac{D(t)}{D_0}\right), \tag{1}$$

while the strain based on the distance (ε_z) between plates is the actuated variable:

$$\varepsilon_z = \ln\left(\frac{L(t)}{L_0}\right). \tag{2}$$

A combination of a PI (proportional/integral) feedback and a feed-forward control is used to act on ε_z to control ε. Hence the evolution of the diameter over time is controlled by changing the plate separation velocity profile accordingly. The governing equations are the following[48]:

$$\varepsilon_z(i+1) = \varepsilon_z(i) + \Delta\varepsilon_z{}^{ff}(i) + K_p[\delta\varepsilon(i) - \delta\varepsilon(i-1)] + K_i\Delta t[\delta\varepsilon(i)], \tag{3}$$

where $\delta\varepsilon$ is the error and $\Delta\varepsilon_z{}^{ff}$ is the feed-forward contribution calculated as:

$$\delta\varepsilon(i) = 2\ln\left(\frac{D(i)}{D_{ideal}(i)}\right), \tag{4}$$

$$\Delta\varepsilon_z{}^{ff}(i) = f(\varepsilon(i+1)) - f(\varepsilon(i)), \tag{5}$$

where $f(\varepsilon)$ describes the kinematic curve (i.e. the relation between the extent of separation between the end plates and the midfilament diameter) with the following function:

$$f(\varepsilon) = \frac{\alpha\varepsilon d}{\alpha\varepsilon + d}, \tag{6}$$

wherein the values of the parameters are $\alpha = 1$ and $d = 2.5$[48]. The actuation time of the system (Δt) is 200 μs. After tuning the proportional and integral gain (K_p and K_i, respectively) of the feedback controller the optimal values found were K_p=0 and K_i=2.5 s^{-1}, in agreement with the values from literature[48]. This results in a deviation from the ideal diameter ranging from approximately 2% at low rates to approximately 15% at strain rates as high as 1 s^{-1}. By increasing the integral gain it is possible to reduce the error and to increase the maximum strain rate at which a successful experiment with closed loop control can be performed. In particular at a value of K_i=12.5 s^{-1} experiments up to $\dot{\varepsilon}$=2.5 s^{-1} are possible. All the experiments shown in this paper are performed with a value of 0 for the proportional gain and 2.5 s^{-1} for the integral gain. Switching off the control loop allows to achieve higher overall strain rates, albeit without control over their local value. More details on the control scheme can be found in the paper of Marín et al.[48].

D. Beamline setup

Time-resolved X-ray experiments have been performed at the Dutch-Belgian beamline (DUBBLE) at the European Synchrotron Radiation Facility (ESRF). Fig. 6 shows the beamline setup.

To allow alignment with respect to the incoming X-ray beam the rheometer is mounted on a system of linear translation stages. For the movements in x and y direction a Huber stage 5102.20

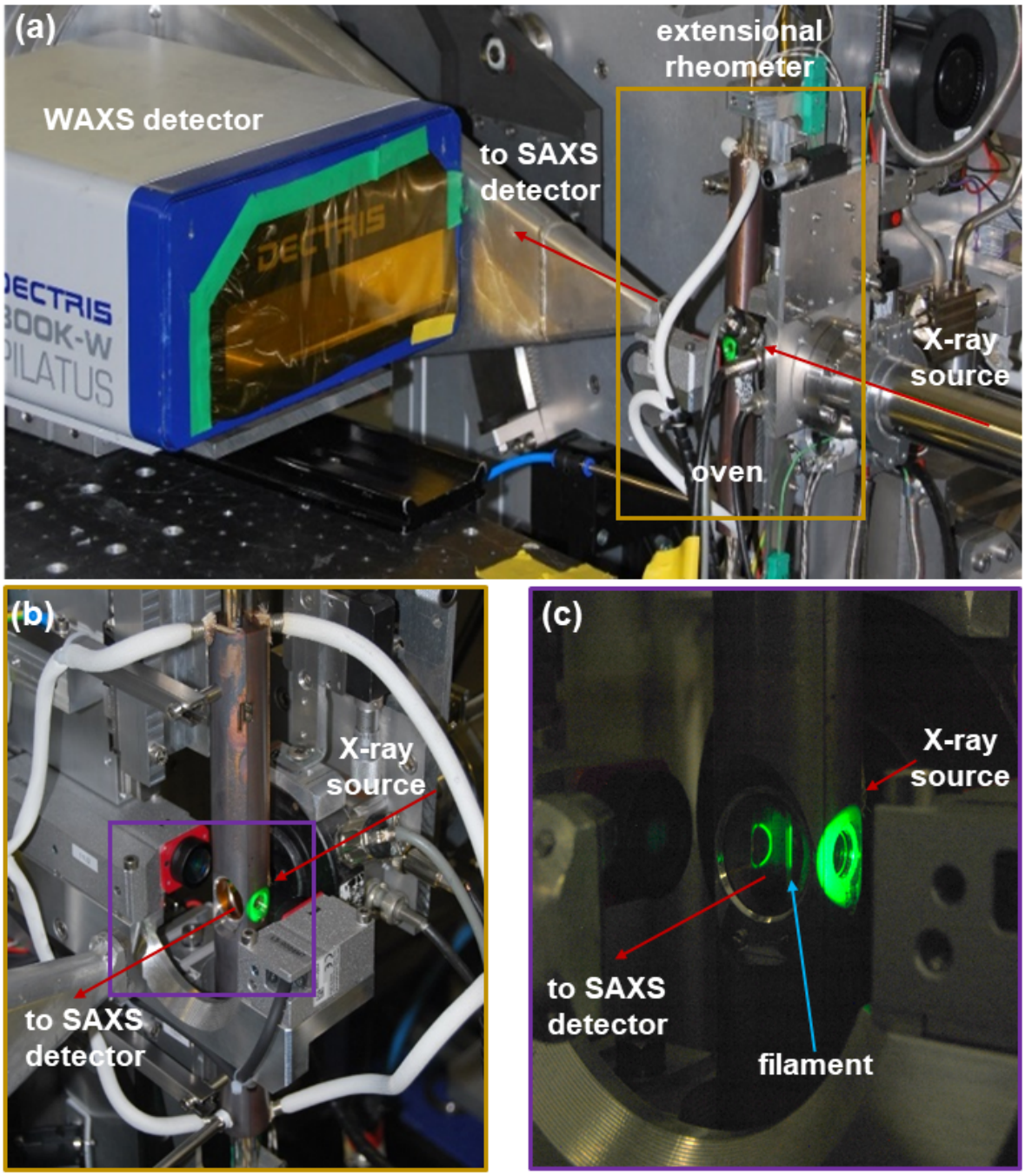

FIG. 6. (a) Experimental setup in the beamline BM26 at ESRF. (b) Close view of the alignment between the oven and the SAXS cone. (c) View of the filament after stretching and complete crystallization.

is used. The travel range of the motor is ± 15 mm and it has a minimal incremental step of 0.1 mm. The z translation stage is a Huber 5103.A20-90 with a travel range of 90 mm and resolution of 0.05 μm. The wavelength of the X-ray beam is 1.0408 Å, and a beam size of 300 μm x 300 μm is obtained by chopping the standard beam. This size is smaller than the minimum value of

TABLE I. Acquisition protocol.

acquisition time [s]	exposure time [s]	delay [s]
60	0.5	-
60	5	-
600	5	25
1080	5	55

the diameter reached during the experiments. During and after extensional flow X-ray scattering (SAXS) and wide angle X-ray diffraction (WAXD) measurements have been performed using, simultaneously, a Pilatus 1M detector (981 x 1043 pixels of 172 μm x 172 μm placed at a distance of 3.432 m) and a Pilatus 300K detector (1472 x 195 pixels of 172 μm x 172 μm placed at a distance of 0.297 m), respectively. The distance and tilt angle were calibrated using AgBe (silver behenate) for the SAXS detector and Al_2O_3 (aluminum oxide) for the WAXD detector. A mask was applied to remove any trace of the beam stop and direct beam from the acquired images that were further corrected for the background and the decrease of the diameter during the experiments[50]. The starting of the SAXS/WAXD acquisition was triggered by an electric TTL pulse send by the rheometer to avoid any time discrepancy. A combination of a fast and a slow acquisition was used to collect both SAXS and WAXD patterns for a total acquisition time of 30 min (1800s). The fast acquisition mode was used in the first 60 s of the experiments and carried out with an exposure time of 0.5 s. For the remaining 1740 s the slow acquisition mode was used, and an exposure time of 5 s was chosen. Detailed information regarding the acquisition procedure can be found in Table I. SAXS and WAXD data were analyzed using the software Fit2D[51] developed by the European Synchrotron Radiation Facility.

III. EXPERIMENTAL PROCEDURE

A. Sample preparation

To validate the performance of the rheometer, experiments on a low density polyethylene (LDPE) (LD 150BW, ExxonMobil) have been carried out. The peak melting temperature (T_m)

of this LDPE is around 112°C, as determined by differential scanning calorimetry (DSC) at a heating rate of 5°C/min. The samples used in our experiments are small LDPE cylinders of 6 mm diameter and 1.5 mm thickness obtained by means of hot compression molding. A rectangular mold was filled with LDPE pellets, heated to 180°C and held at this temperature for 5 min. Subsequently a force of 250 kN was applied and held for 6 min allowing the molten polymer to be shaped between the two hot plates. After cooling to room temperature, samples of the desired dimensions were punched out of the polymer sheet. A schematic of the procedure for the extensional rheology experiment is shown in Fig. 7. The compression molded sample is placed on the bottom plate allowing for melting. The plates are then moved close to each other, thereby slightly compressing the molten polymer to ensure attachment to both plates before surface tension effects become predominant. The sample is held in between the plates for a sufficient time allowing relaxation and homogenization of the temperature. Subsequently, the material is slowly prestretched to a desired midfilament diameter value and its complete relaxation. During this procedure a small flow could be present due to the interfacial tension and viscoelastic relaxation of the material, causing a small decrease of the filament diameter. Moreover, depending on the viscosity of the material, the height of the midpoint could shift to a lower position because of gravitational effects. Both phenomena are visible on the real time video images from the laser micrometer, thus making it possible to realign the midpoint to the center of the laser by moving both plates simultaneously in the same direction. The midpoint position during both the prestretch and the experiment is constantly monitored, indicating a fixed position for all the experiments performed in this work. In the rest of the manuscript we will refer to $\Lambda_i = L_i/D_i$ as the initial aspect ratio of the compression molded sample, $\Lambda_c = L_c/D_c$ as the aspect ratio prior to the prestretch and L_0 and D_0 as the values right before starting the experiment, of the length L (distance between the plates) and the midfilament diameter D (measured with the laser micrometer) that will be used in the control loop as initial conditions.

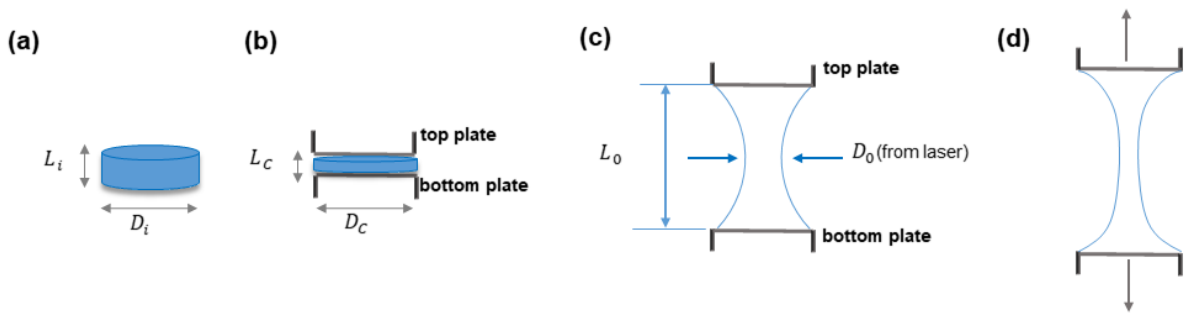

FIG. 7. Schematic of the experimental procedure. (a) Preparation of the sample by compression molding. (b) Melting and attachment to the end plates, by slight compression. (c) Prestretching. (d) Controlled uniaxial deformation.

B. Linear viscoelasticity

The material response to extensional flow is different from the one in simple shear. This is because extensional flow is irrotational and, therefore, it can induce much stronger orientation and stretching of the macromolecules. In a uniaxial extensional deformation the material function of interest is the transient extensional viscosity that is a function of the extension rate, time and temperature. For viscoelastic fluids after startup of the flow only in the limit of very low extension rates the transient extensional viscosity approaches three times the transient shear viscosity, thereby defining the linear viscoelastic envelope (LVE)[52]. At higher strain rates, for branched polymers as LDPE, the extensional viscosity deviates upwards from the LVE, and this phenomenon is known as "strain hardening"[45,49,53]. The linear viscoelastic behavior of the LDPE was determined using small amplitude oscillatory shear (SAOS) measurements. A 25 mm plate-plate geometry was mounted on an ARES rheometer with a convection oven using a nitrogen flux and experiments at four different temperatures, between 130°C and 190°C, were performed at 2% strain. The data were shifted to a master curve at the reference temperature of 150°C using time-temperature-superposition (TTS) (Fig. 8 (a)). The shift factors (Fig. 8 (b)) were fitted with the Arrhenius equation[54]:

$$a_{\mathrm{T}} = \exp\left[\frac{E_{\mathrm{a}}}{R}\left(\frac{1}{T} - \frac{1}{T_{\mathrm{ref}}}\right)\right]. \tag{7}$$

In the above equation the fitting parameter is the activation energy E_{a}, R is the universal gas constant, T the temperature and T_{ref} the reference temperature. Good agreement between the

TABLE II. Relaxation spectrum for LDPE at 150°C.

mode	λ_i [s]	G_i [Pa]
1	0.00406	$1.44 \cdot 10^5$
2	0.0461	$4.85 \cdot 10^4$
3	0.386	$2.09 \cdot 10^4$
4	3.04	$7.46 \cdot 10^3$
5	22.7	$1.84 \cdot 10^3$
6	170	224

fitting and the experimental shift factors is found for a value of E_a of 65.7 kJ/mol, which is in agreement with literature values for a different LDPE grade[55].

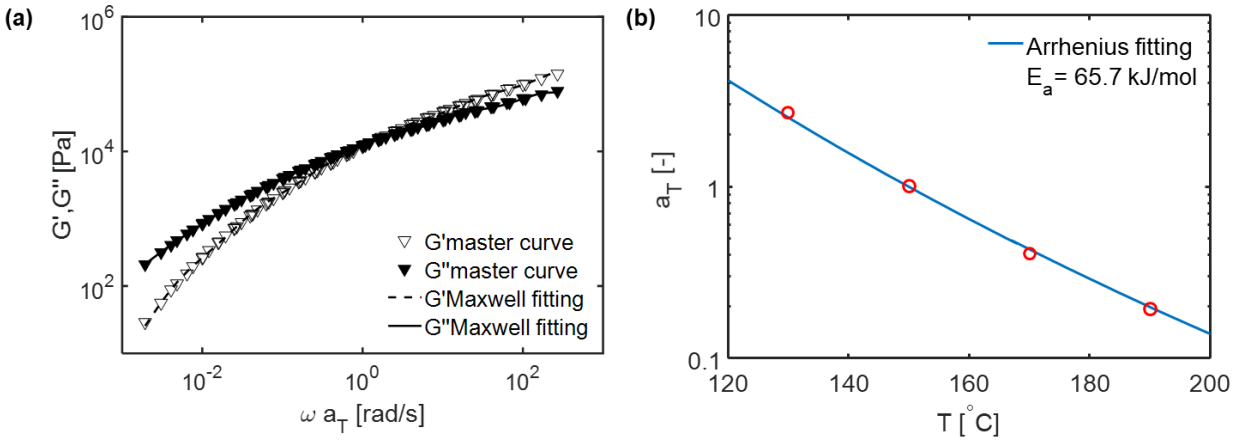

FIG. 8. (a) Master curve of storage modulus G' (open symbols) and loss modulus G'' (filled symbols) at the reference temperature of 150°C and multi-mode Maxwell model fitting (dashed and continuous lines). (b) Time-temperature shift factors (open symbols) and Arrhenius fitting.

A multi-mode Maxwell model was fitted on the dynamic moduli to obtain the linear viscoelastic relaxation spectrum. This model is constructed by placing n modes in parallel, whereby each mode (a spring and a dashpot connected in series) models a viscoelastic contribution of the polymer. The relaxation times and corresponding plateau moduli for LDPE are given in Table II.

C. Experimental procedure for *in-situ* X-ray experiments

To perform *in-situ* structure characterization experiments it is important that the midfilament point is perfectly aligned with the X-ray beam. After the polymer has been prestretched, the temperature is lowered to the desired experimental value. Before the temperature reaches the set point an X-ray scan is performed by moving the rheometer along the x- and z- direction, allowing the material, during this aligning procedure, to achieve the experimental temperature. During this process the reduction of the minimum diameter was negligible (around 2%). The transmitted beam intensity collected at the photo-diode is used to evaluate the coordinates of the midfilament point. Fig. 9 (a) illustrates the alignment method.

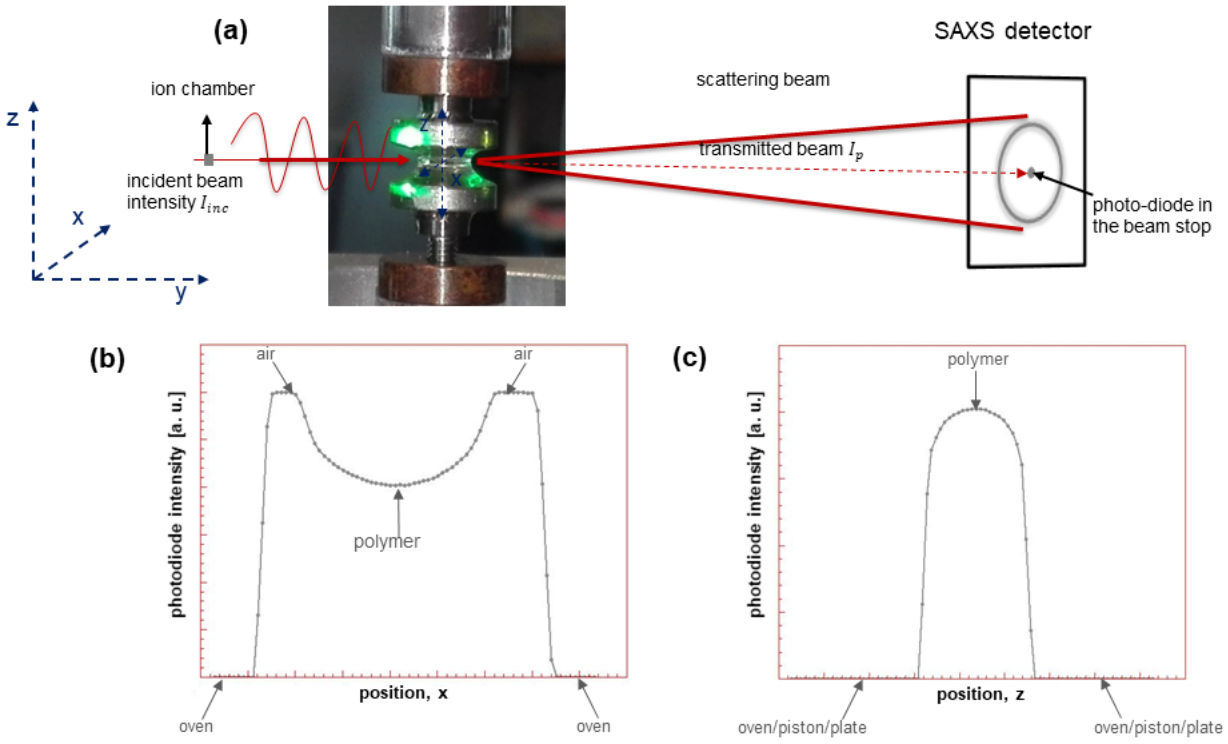

FIG. 9. (a) Schematic of the scanning procedure to find the midfilament point. (b) Photo-diode intensity profile in horizontal direction. (c) Photo-diode intensity profile in vertical direction.

When scanning along the x-direction (i.e. along the width of the sample) the metal of the oven initially absorbs the complete intensity received, as a consequence no intensity is transmitted to the photo-diode. Moving further the intensity suddenly reaches a maximum, corresponding to the air present in the oven. A subsequent decrease of the transmission marks the presence of

the polymer which absorbs part of the intensity proportionally to its thickness. The minimum in the intensity profile at the photo-diode corresponds to the center of the polymer, the profile is symmetric because of the geometry of the prestretched sample. While scanning along the z-direction (i.e. along the height of the sample) the photo-diode intensity is only different from zero when the X-rays pass through the polymer and the intensity shows a maximum at the midfilament region where the thickness is the lowest. Fig. 9 (b) and Fig. 9 (c) show the transmitted intensity profile, as measured with the photo-diode, as a function of the scanning position. This procedure allows to precisely identify the midfilament point and to align it to the X-ray beam source. A quiescent experiment (no flow applied after the prestretch) has been performed prior to the flow experiment to determine the time window for the temperature stabilization and scanning procedure before the polymer starts to crystallize. In quiescent conditions the crystallization starts around 200s after the completion of thermal homogenization and alignment. The scanning procedure takes less than 5 minutes during which, SAXS/WAXD patterns of the midfilament region have been acquired to check that the material remains amorphous.

IV. RESULTS AND DISCUSSION

A. Control scheme and melt rheology validation

To demonstrate the capability of our rheometer to locally control the deformation, the implementation of the control scheme was validated by performing experiments at different flow conditions. Fig. 10 (a) demonstrates that the laser measurement effectively occurs at the point of minimum diameter. In Fig. 10 (b) we report the evolution of the diameter in time in comparison with the ideal exponential decrease during representative experiments performed at strain rates of 0.1 s^{-1} and 1 s^{-1}, and a temperature of 150°C for an LDPE sample. Fig. 10 (c) shows the non-ideal relation between the strains in axial and radial directions.

The transient extensional viscosity calculated from a force balance[56], and in absence of surface tension and inertia contributions, is defined as[44,57]:

$$\eta_E{}^+ = \frac{F_z - 1/2mg}{\dot{\varepsilon}\pi D^2/4}(\kappa_{\dot{\gamma}}). \tag{8}$$

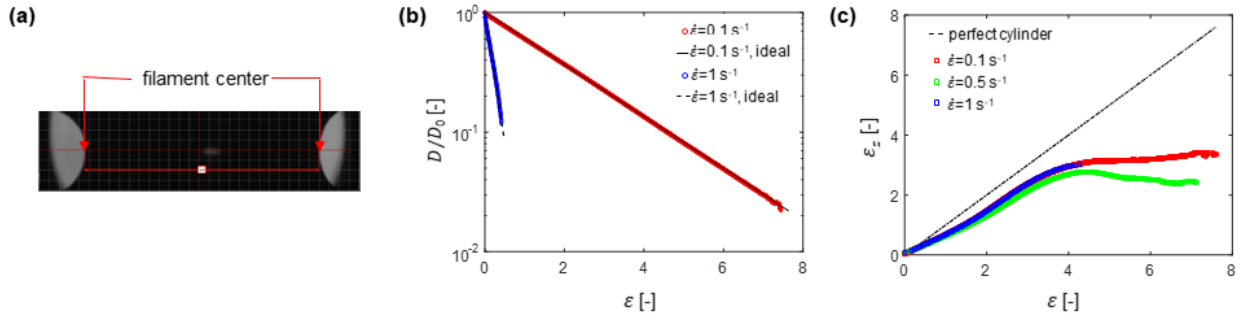

FIG. 10. (a) Optical image of the area around the filament point. (b) Comparison of the evolution of the filament diameter with the ideal exponential thinning profile. (c) Kinematic curve for the evolution of the axial strain. Experiments with LDPE at a temperature of 150°C.

In the above equation F_z is the axial force measured by the load cell, g is the gravitational acceleration, m the mass of the filament, D the diameter measured with the laser micrometer and $\dot{\varepsilon}$ the strain rate. At the startup of the flow strong shear contributions can be generated due to the pinning of the polymer at the end plates. The consequent radial pressure gradient adds an extra contribution to the axial force measured that can be compensated for by using a correction factor[58]:

$$\kappa_{\dot{\gamma}} = \left(1 + \frac{\exp(-7\left(\varepsilon + \varepsilon_{pre}/3\right))}{3{\Lambda_c}^2}\right)^{-1}. \tag{9}$$

The above expression takes into account the amount of deformation that the polymer undergoes during the prestretch (ε_{pre}) and the aspect ratio prior to it (Λ_c). For large strains the shear contribution becomes negligible because of the reduction of the radial pressure gradients[59].

To test the validity of the rheological data, the extensional viscosity measured with our rheometer (rheoTU/e) has been compared with the linear viscoelastic envelope (LVE) and the extensional viscosity, measured at the same flow and temperature conditions, with a Sentmanat Extensional Rheometer (SER) setup mounted on an Anton Paar MCR502 with convection oven. The linear viscoelastic envelope is calculated from the following equation[52]:

$${\eta_E}^+ = 3\sum_i G_i\lambda_i\left(1 - \exp\left(\frac{-t}{\lambda_i}\right)\right). \tag{10}$$

Fig. 11 shows that the rheological response measured with our rheometer for LDPE is in nice agreement with the linear viscoelastic envelope (LVE) in the linear region and with data from the

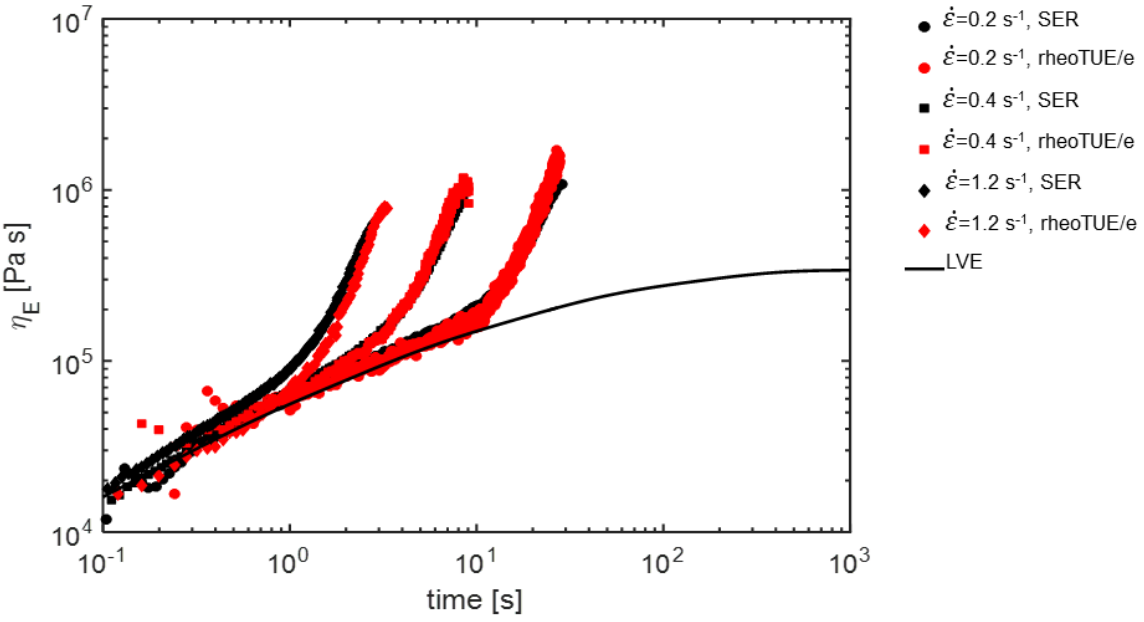

FIG. 11. Measured extensional viscosity as a function of time for LDPE at 150°C at different strain rates, comparison with SER measurements and LVE envelope.

commercial device (SER) over the complete measurement range.

B. Combining rehology and *in-situ* SAXS/WAXD

To demonstrate the potential of our filament stretching rheometer for *in-situ* structure characterization, time-resolved X-ray experiments have been performed while applying a locally controlled deformation. A case study experiment is reported at 107°C, for a strain rate of 1.2 s^{-1} and final strain of 3.2. Fig. 12 demonstrates that the crystallization kinetics, and the evolution of the crystal structure and morphology, during and after uniaxial extension, can be studied with our rheometer. The scattering patterns collected during flow (Fig. 12 (a)) being characteristics of the shish-kebab evolution can be compared to the viscosity evolution, which is measured simultaneously. In the linear regime the polymer is amorphous and no scattering pattern is observed. When the viscosity deviates from the LVE envelope, streaks appear in the SAXS pattern in the direction perpendicular to the flow, indicating the formation of shish. Immediately after the shish form, and the deformation proceeds, lobes due to the scattering of crystal lamellae (kebabs) start to grow on top of the

shish as is clearly visible from the increase of the scattered intensity in the direction of the flow.

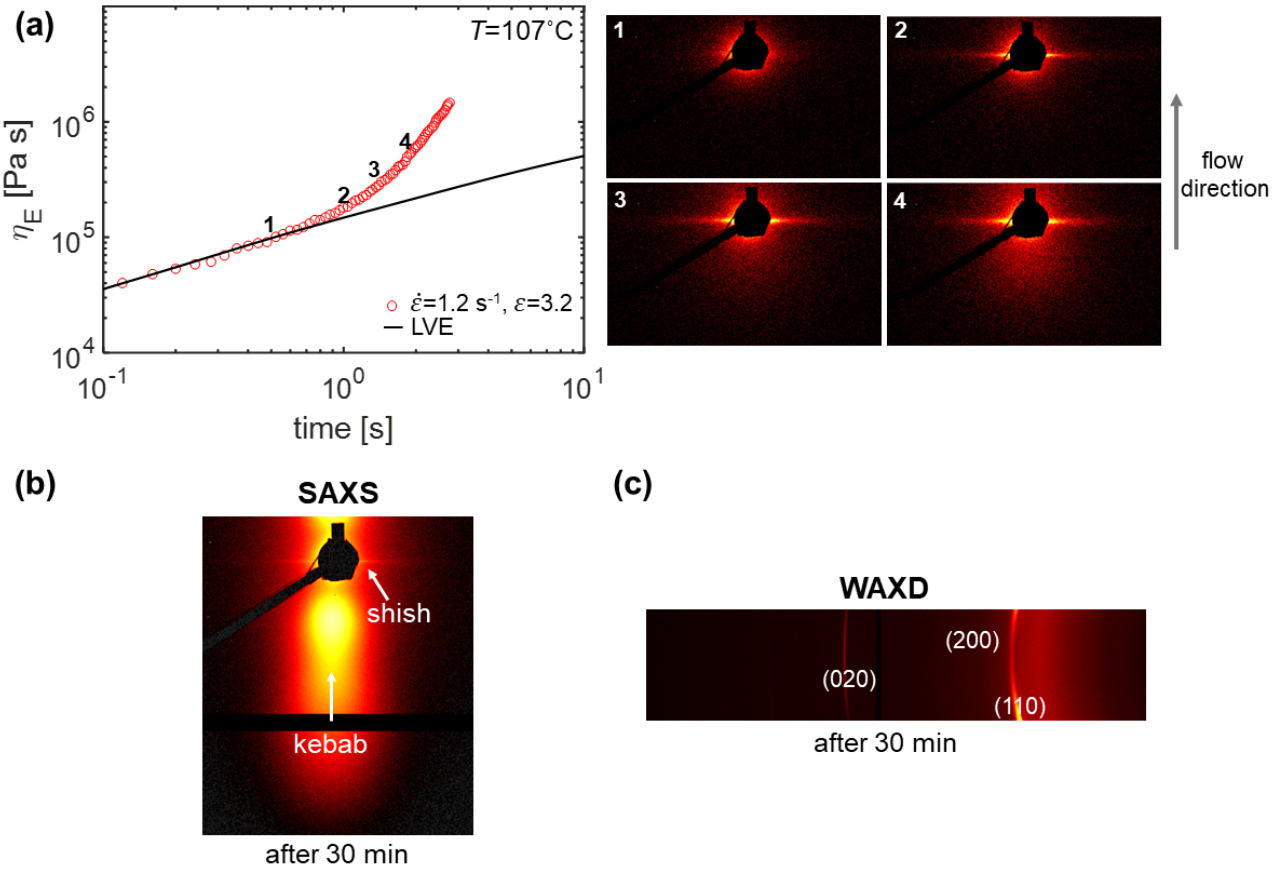

FIG. 12. (a) Shish kebab morphology evolution and extensional rheology response during flow, at a strain rate of 1.2 s^{-1} and final Hencky strain of 3.2. (b) SAXS pattern and (c) 1D-WAXD pattern after cessation of flow and complete crystallization (after 30 min). The positions of shish, kebabs and of the characteristic crystal peaks of LDPE are indicated on the scattering and diffraction pattern, respectively.

To gain a better understanding of the changes in the morphology of the crystalline structures, an analysis of the intensity scattered at small angles was carried out. From the 2D-SAXS pattern two azimuthal regions can be identified. The equatorial (centered at ϕ=0°), and meridional (centered at ϕ=90°) (Fig. 13 (a)), where scattering of respectively shish and kebabs occurs. To obtain the time evolution of the intensity the 2D-SAXS pattern was integrated azimuthally in both regions according to:

$$I_{\mathrm{SAXS}} = \int_{q_{\min}}^{q_{\max}} \int_{\phi_{\min}}^{\phi_{\max}} I(\phi, q)\, d\phi\, dq, \tag{11}$$

where q_{min} and q_{max} are the minimum and maximum values of the scattering vector experimentally accessible, ϕ_{min} and ϕ_{max} are the minimum and maximum value of the azimuthal angle (for the meridional region ϕ_{min}=45° and ϕ_{max}=135°, for the equatorial region ϕ_{min}=-15° and ϕ_{max}=20°. Because the beam stop is not perfectly aligned to the shish position, the integration area of the equatorial region results to be asymmetrical). The intensities of the kebab (flow experiment) and of the spherulites (quiescent experiment) have been corrected with the Lorentz factor for a 2D and 3D object respectively[60]. The time evolution of the SAXS meridional and equatorial intensity is reported in Fig. 13. The intensities are normalized with respect to the corresponding maximum values (to allow a more clear comparison of the trends in Fig. 13 (b)). The kebabs intensity is compared with the scattered intensity under quiescent conditions. As expected flow has two main effects on the crystallization process. Firstly, it enhances the crystallization rate, an effect which is noticeable from the earlier onset of crystallization and the quasi-plateau reached in the meridional intensity curve compared to the quiescent case. Secondly, it modifies the crystallization kinetics changing the shape of the intensity curve versus time, due to the development of highly oriented structures. Furthermore it can be observed that the equatorial intensity (shish) grows much faster during flow as compared to the meridional one (kebab) and it shows an unusual maximum followed by a decrease over time. We believe that this phenomenon is caused by the nature of the SAXS technique itself. The scattered intensity indicates the deviation of the local electron density from the average electron density in the irradiated volume[61], as a consequence, when kebabs start to grow very fast they take over the shish on the scattering pattern causing, because of the electron density difference, an apparent decrease of the equatorial intensity.

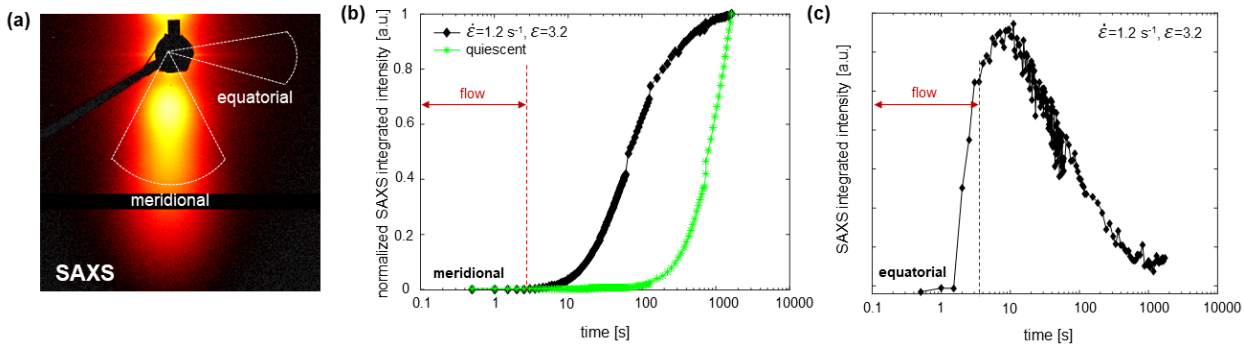

FIG. 13. (a) Anisotropic two-dimensional SAXS image showing the two azimuthal regions. (b) Kebab intensity evolution (black) compared with meridional intensity evolution under quiescent conditions (green). (c) Shish intensity evolution.

Simultaneously 1D-WAXD patterns have been acquired in the equatorial direction. Because the Pilatus 300K detector has a limited azimuthal range (not sufficient to capture the complex orientation and twisted lamellae typical of polyethylene[62]) only a qualitative time evolution of the characteristic crystal peaks of LDPE is provided. The 3D-plot in Fig. 14 shows the intensity profiles obtained by radially integrating the 1D-pattern and plotting it against the time and the scattering angle (2θ). The evolution from a completely molten polymer, at the start of the flow, to a fully crystallized one starts with the decrease of the amorphous halo and the appearance of the characteristic peak (110) approximately after 2.5 s. Three reflections centered at scattering angle values (2θ) of 14.7°, 15.1° and 25.4° related to interplanar distances (d) of 4.1 Å , 3.9 Å and 2.4 Å , characteristic for the (110), (200) and (020) planes of the orthorhombic form of polyethylene[63], respectively are present. The small peak at lower scattering angle could suggest the presence of the (001) plane of the monoclinic form of polyethylene usually favored by high deformations[64]. The investigation of the latter is outside the scope of this work.

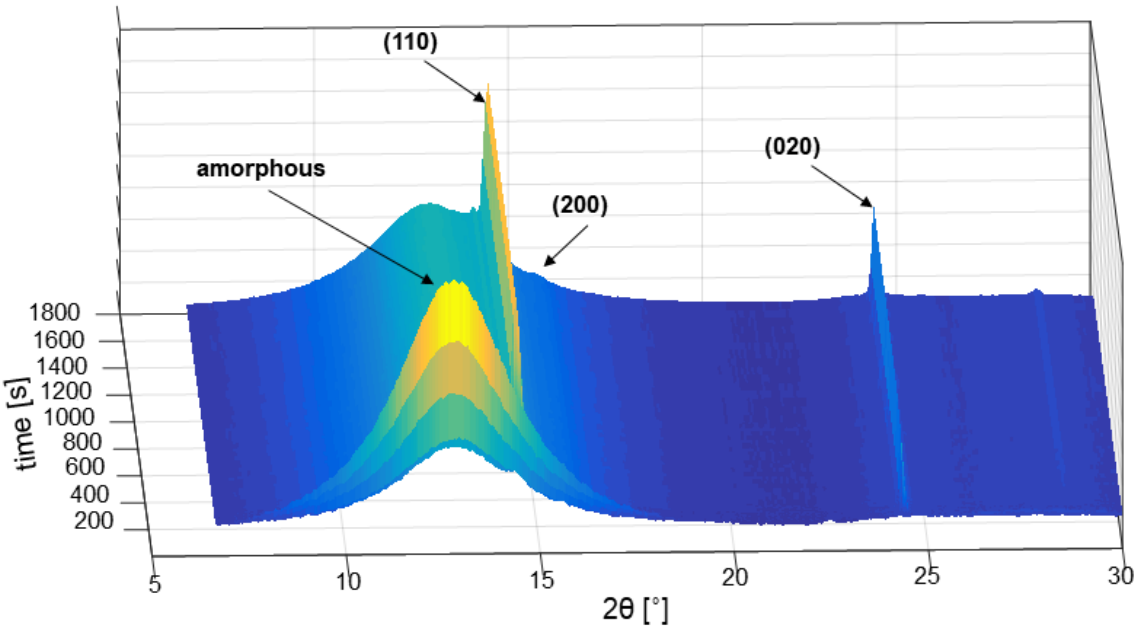

FIG. 14. Real-time 1D-WAXD evolution for the experiment performed at a final Hencky strain of 3.2 with a constant strain rate of 1.2 s^{-1}.

The results from this case study on LDPE demonstrate the capability of our in-house developed rheometer to simultaneously capture the structure and morphology evolution, and thus the kinetics of the development of the microstructure, while the polymer undergoes a controlled uni-

axial extensional deformation. Further experiments at different flow conditions, and on different semi-crystalline polymers, will help in unraveling unsolved questions of flow induced crystallization. Furthermore the fixed location of the midfilament point is a unique innovation that makes the device flexible towards different *in-situ* characterization techniques.

V. CONCLUSIONS

A filament stretching rheometer has been designed and constructed, with the ability to perform *in-situ* X-ray experiments on flow-induced crystallization of polymer melts during and after a precisely controlled uniaxial extensional flow. To demonstrate the performance of the rheometer the extensional rheology of a molten LDPE sample has been measured, and *in-situ* flow induced crystallization experiments have been performed in a synchrotron radiation facility. Controlled experiments with extension rates up to 2.5 s^{-1}, with a deviation from the ideal diameter ranging from 2% to approximately 15%, depending on the applied strain rate and chosen controller gains, are possible and good agreement with results from commercial rheometers is found. Furthermore the *in-situ* X-ray experiments demonstrate that the crystallization kinetics, and the evolution of crystal structure and morphology can be studied with our innovative rheometer. Access to this unique information will help us to develop an enhanced understanding of extensional flow-induced crystallization that is essential for the design of polymer processing operations involving extensional flow. The flexibility of the rheometer towards different *in-situ* characterization techniques, due to the steady location of the midfilament point, opens new opportunities in material testing.

SUPPLEMENTARY MATERIAL

See supplementary material for the 3D virtual reality model of the in-house filament stretching rheometer.

ACKNOWLEDGMENTS

This work forms part of the research program of the Brightlands Materials Center (BMC). We acknowledge the European Synchrotron Radiation Facility (ESRF) for provision of synchrotron radiation facilities and NWO for financing beamtime at ESRF. We would like to thank Leon Govaert for providing the LDPE polymer. We thank Ole Hassager and Qian Huang for the training on filament stretching rheometer measurements at the Technical University of Denmark (DTU).

DATA AVAILABILITY STATEMENT

The data that support the findings of this study are available from the corresponding author upon reasonable request.

REFERENCES

[1]H. Janeschitz-Kriegl, *Crystallization modalities in polymer melt processing* (Springer, 2018).

[2]R. H. Somani, L. Yang, L. Zhu, and B. S. Hsiao, Polymer **46**, 8587–8623 (2005).

[3]F. De Santis, R. Pantani, and G. Titomanlio, Polymer **90**, 102–110 (2016).

[4]H. J. M. Caelers, L. E. Govaert, and G. W. M. Peters, Polymer **83**, 116–128 (2016).

[5]K. Bernland, T. Tervoort, and P. Smith, Polymer **50**, 2460–2464 (2009).

[6]J. Gomes, J. S. Nunes, V. Sencadas, and S. Lanceros-Méndez, Smart Materials and Structures **19**, 065010 (2010).

[7]S. Liedauer, G. Eder, H. Janeschitz-Kriegl, P. Jerschow, W. Geymayer, and E. Ingolic, International Polymer Processing **8**, 236–244 (1993).

[8]J. Baert, P. V. Puyvelde, and F. Langouche, Macromolecules **39**, 9215–9222 (2006).

[9]H. Janeschitz-Kriegl, E. Ratajski, and M. Stadlbauer, Rheologica acta **42**, 355–364 (2003).

[10]G. Kumaraswamy, A. M. Issaian, and J. A. Kornfield, Macromolecules **32**, 7537–7547 (1999).

[11]M. Seki, D. W. Thurman, J. P. Oberhauser, and J. A. Kornfield, Macromolecules **35**, 2583–2594 (2002).

[12]J.-B. Boitte, C. Vizcaïno, L. Benyahia, J.-M. Herry, C. Michon, and M. Hayert, Review of Scientific Instruments **84**, 013709 (2013).

[13]N. Y. Lin, J. H. McCoy, X. Cheng, B. Leahy, J. N. Israelachvili, and I. Cohen, Review of

Scientific Instruments **85**, 033905 (2014).

[14]R. H. Somani, B. S. Hsiao, A. Nogales, S. Srinivas, A. H. Tsou, I. Sics, F. J. Balta-Calleja, and T. A. Ezquerra, Macromolecules **33**, 9385–9394 (2000).

[15]L. Balzano, S. Rastogi, and G. W. M. Peters, Macromolecules **41**, 399–408 (2008).

[16]L. Balzano, Z. Ma, D. Cavallo, T. B. van Erp, L. Fernandez-Ballester, and G. W. M. Peters, Macromolecules **49**, 3799–3809 (2016).

[17]J. Chang, Z. Wang, X. Tang, F. Tian, K. Ye, and L. Li, Review of Scientific Instruments **89**, 025101 (2018).

[18]E. M. Troisi, H. J. M. Caelers, and G. W. M. Peters, Macromolecules **50**, 3868–3882 (2017).

[19]E. M. Troisi, M. van Drongelen, H. J. M. Caelers, G. Portale, and G. W. M. Peters, European Polymer Journal **74**, 190–208 (2016).

[20]P. Hejmady, L. C. Cleven, L. C. van Breemen, P. D. Anderson, and R. Cardinaels, Review of Scientific Instruments **90**, 083905 (2019).

[21]G. Portale, D. Cavallo, G. C. Alfonso, D. Hermida-Merino, M. v. Drongelen, L. Balzano, G. W. M. Peters, J. G. P. Goossens, and W. Bras, Journal of applied crystallography **46**, 1681–1689 (2013).

[22]B. Luijsterburg, P. Jobse, D. Hermida Merino, T. Peijs, and H. Goossens, Journal of Polymer Science Part B: Polymer Physics **52**, 1071–1082 (2014).

[23]G. Portale, D. Hermida-Merino, and W. Bras, European Polymer Journal **81**, 415–432 (2016).

[24]A. J. Ryan, W. Bras, D. Hermida-Merino, and D. Cavallo, Journal of Non-Crystalline Solids **451**, 168–178 (2016).

[25]S. Filipe, B. Knogler, K. Buchmann, and M. Obadal, Journal of thermal analysis and calorimetry **98**, 667–674 (2009).

[26]M. Chellamuthu, D. Arora, H. H. Winter, and J. P. Rothstein, Journal of Rheology **55**, 901–920 (2011).

[27]M. Sentmanat, O. Delgadillo-Velázquez, and S. G. Hatzikiriakos, Rheologica Acta **49**, 931–939 (2010).

[28]M. Derakhshandeh and S. G. Hatzikiriakos, Rheologica Acta **51**, 315–327 (2012).

[29]C. Hadinata, D. Boos, C. Gabriel, E. Wassner, M. Rüllmann, N. Kao, and M. Laun, Journal of Rheology **51**, 195–215 (2007).

[30]E. E. B. White, H. H. Winter, and J. P. Rothstein, Rheologica acta **51**, 303–314 (2012).

[31]P. C. Roozemond and G. W. M. Peters, Journal of Rheology **57**, 1633–1653 (2013).

[32]S. L. Wingstrand, M. van Drongelen, K. Mortensen, R. S. Graham, Q. Huang, and O. Hassager, Macromolecules **50**, 1134–1140 (2017).

[33]S. L. Wingstrand, L. Imperiali, R. Stepanyan, and O. Hassager, Polymer **136**, 215–223 (2018).

[34]M. Kisilak, H. Anderson, N. S. Babcock, M. R. Stetzer, S. H. Idziak, and E. B. Sirota, Review of Scientific Instruments **72**, 4305–4307 (2001).

[35]F. H. M. Swartjes, G. W. M. Peters, S. Rastogi, and H. E. H. Meijer, International Polymer Processing **18**, 53–66 (2003).

[36]J. van Meerveld, G. W. M. Peters, and M. Hütter, Rheologica Acta **44**, 119–134 (2004).

[37]T. Hu, N. Tian, S. Ali, Z. Wang, J. Chang, N. Huang, and L. Li, Langmuir **32**, 2117–2126 (2016).

[38]Z. Wang, F. Su, Y. Ji, H. Yang, N. Tian, J. Chang, L. Meng, and L. B. Li, Journal of Rheology **61**, 589–599 (2017).

[39]Z. Wang, J. Ju, L. Meng, N. Tian, J. Chang, H. Yang, Y. Ji, F. Su, and L. Li, Soft matter **13**, 3639–3648 (2017).

[40]Y. Liu, W. Zhou, K. Cui, N. Tian, X. Wang, L. Liu, L. Li, and Y. Zhou, Review of Scientific Instruments **82**, 045104 (2011).

[41]M. L. Sentmanat, Rheologica acta **43**, 657–669 (2004).

[42]E. M. McCready and W. R. Burghardt, Journal of Rheology **59**, 935–956 (2015).

[43]V. Tirtaatmadja and T. Sridhar, Journal of Rheology **37**, 1081–1102 (1993).

[44]S. H. Spiegelberg, D. C. Ables, and G. H. McKinley, Journal of Non-Newtonian Fluid Mechanics **64**, 229–267 (1996).

[45]G. H. McKinley and T. Sridhar, Annual Review of Fluid Mechanics **34**, 375–415 (2002).

[46]A. Bach, H. K. Rasmussen, and O. Hassager, Journal of Rheology **47**, 429–441 (2003).

[47]N. Orr and T. Sridhar, Journal of Non-Newtonian Fluid Mechanics **82**, 203–232 (1999).

[48]J. M. R. Marín, J. K. Huusom, N. J. Alvarez, Q. Huang, H. K. Rasmussen, A. Bach, A. L. Skov, and O. Hassager, Journal of Non-Newtonian Fluid Mechanics **194**, 14–22 (2013).

[49]S. L. Anna, C. Rogers, and G. H. McKinley, Journal of Non-Newtonian Fluid Mechanics **87**, 307–335 (1999).

[50]H. J. M. Caelers, E. M. E. Troisi, L. E. Govaert, and G. W. M. Peters, Polymers **9**, 547 (2017).

[51]A. Hammersley, Journal of Applied Crystallography **49**, 646–652 (2016).

[52]C. W. Macosko and R. G. Larson, "Rheology: principles, measurements, and applications," (1994).

[53]G. Liu, H. Sun, S. Rangou, K. Ntetsikas, A. Avgeropoulos, and S.-Q. Wang, Journal of Rheology **57**, 89–104 (2013).

[54]C.-Y. Liu, J. He, R. Keunings, and C. Bailly, Macromolecules **39**, 8867–8869 (2006).

[55]Q. Huang, M. Mangnus, N. J. Alvarez, R. Koopmans, and O. Hassager, Rheologica Acta **55**, 343–350 (2016).

[56]P. Szabo, Rheologica Acta **36**, 277–284 (1997).

[57]M. Yao and G. H. McKinley, Journal of Non-Newtonian Fluid Mechanics **74**, 47–88 (1998).

[58]J. K. Nielsen, H. K. Rasmussen, and O. Hassager, Journal of Rheology **52**, 885–899 (2008).

[59]M. I. Kolte, H. K. Rasmussen, and O. Hassager, Rheologica Acta **36**, 285–302 (1997).

[60]M. Tolan and M. Tolan, *X-ray scattering from soft-matter thin films: materials science and basic research* (Springer, 1999).

[61]N. Stribeck, *X-ray scattering of soft matter* (Springer Science & Business Media, 2007).

[62]M. van Drongelen, D. Cavallo, L. Balzano, G. Portale, I. Vittorias, W. Bras, G. C. Alfonso, and G. W. M. Peters, Macromolecular materials and engineering **299**, 1494–1512 (2014).

[63]A. Turner-Jones, Journal of Polymer Science **62**, S53–S56 (1962).

[64]M. M. H. Shirazi, M. Khajouei-Nezhad, S. M. Zebarjad, and R. Ebrahimi, Polymer Bulletin **77**, 1681–1694 (2020).